J. Comput. Appl. Res. Mech. Eng. Vol. 11. No. 1, pp. 227-242, 2021 *DOI: 10.22061/JCARME.2020.4871.1596*

Journal of Computational and Applied Research in Mechanical Engineering
jcarme.sru.ac.ir
SRTTU
JCARME
ISSN: 2228-7922

Research paper

Tomographic reconstruction of isotropic materials using genetic algorithms with ultrasound time-of-flight projection data

Shyam Prasad Kodali and Boggarapu Nageswara Rao*

Department of Mechanical Engineering, Koneru Lakshmaiah Education Foundation, Vaddeswaram, A.P., India, 522502

Article info:

Article history:

Received:	22/02/2019
Revised:	03/05/2020
Accepted:	06/05/2020
Online:	09/05/2020

Keywords:

Non destructive evaluation,
Tomography,
Tomographic reconstruction,
Genetic algorithms,
Ultrasound time of flight.

***Corresponding author:**
bnrao52@rediffmail.com

Abstract

Engineering materials and structures have crack-like defects leading to premature failures. The usage of fracture mechanics to assess the structural integrity requires knowledge on the type, location, shape, size, and orientation of the flaws. Tomographic reconstruction is one of the commonly used nondestructive testing methods for flaw characterization. The cross sectional image of the object being tested is obtained through the application of various reconstruction methods that are categorized as either analytical methods or iterative methods. In this work, an iterative algorithm that works on the principles of genetic algorithms is developed and used for the reconstruction. The results of simulation studies on the tomographic reconstructions using genetic algorithms for the identification of defects in isotropic materials are discussed in the paper. The solution methodology based on the use of genetic algorithms is applied to reconstruct the cross sections of test specimens with different flaw characteristics. Simulated time-of-flight data of ultrasound rays transmitted through the specimen under investigation is used as input to the algorithm. The time-of-flight data is simulated neglecting the bending of ultrasound rays and assuming straight ray paths. Numerical studies performed on several specimens with flaws of known materials but unknown location, size and shape are presented. The number of ultrasonic transmitters and receivers needed for complete scanning of the specimen's cross section is analyzed and presented. The findings of the parametric analysis and sensitivity analysis in order to choose appropriate range of algorithm parameters for performance quality and robustness of the algorithm are presented. The performance of the present algorithm with noisy projection data is also discussed.

1. Introduction

In many real world applications one needs to have an idea of the internal structure of a given object without ravaging the object. For example, medical personnel require diagnosing the health condition of the internal organs in a non-invasive manner. On similar lines, an aircraft needs to be thoroughly inspected for its structural integrity at regular intervals of time for being certified as flight worthy. This is not just a desirable feature

but a compulsion to get sanction from authorities like the safety and quality assurance [1]. As a matter of fact, all types of engineering materials and engineering structures have some form of defects or flaws which may eventually lead to catastrophic failures. In view of the above, engineers are interested in assessing the presence of internal defects in engineering materials and structures through non-destructive evaluation (NDE) methods. Fracture mechanics helps the structural integrity assessment of engineering materials and structures considering the flaw characteristics like the type, location, shape, size, and orientation of the flaws. Computed tomography (CT) is widely used as a non-invasive method with different reconstruction methodologies. In this work, an enhanced reconstruction procedure based on the application of genetic algorithms [2] is proposed and tested for various possibilities of flaws in engineering materials and structures prior to the recommendation of tomographic reconstruction with genetic algorithms.. The proposed methodology works on the collection of ultrasound time-of-flight (TOF) as the projection data and the application of genetic algorithms for detecting the presence of multiple inclusions of known physical properties in a given test specimen. Specifically the number, shape, size and location of inclusions can be acquired.

The goal of tomography is to use projections in order to estimate the distribution of material densities across the cross-section of an object in a nondestructive manner. The projections are obtained from suitable energy interactions with the object and the material distribution is visualized as an image which mathematically is represented as a function f(x, y) [3]. The process is technically referred to as reconstruction. Tomography is thus an inverse problem and the process of solving this inverse problem is called image reconstruction. CT has been in utilization in medical settings since the 1970s and in recent times there is an ongoing interest in the industrial applications like NDE of fabricated steel structures, electronic circuit boards, multi phase fluid flows, homeland security, nuclear fuel assemblies, food packaging, and reinforced concrete structures [4-9]. The mathematical basis for tomographic imaging was laid down by Johann Radon in 1917, who showed that an exact representation of an object can be obtained from a complete set of its projections. This mathematical process called the Radon transform has become the basis for X-ray tomography, that is also used in geophysics [10]. This latter application used stress wave velocities in solid materials, and accordingly can be additionally utilized as a part of the recognition of deformities in structural materials. With reference to NDE of engineering materials, tomography is a method for looking through an object in order to visualize the characteristics (shape, size and location) of defects inside the object. As the technique is non-invasive in nature, the cross-section images of an object can be obtained without causing any damage to the structural integrity of the object being investigated. To accomplish this, a specific physical property of the materials involved is estimated using projection data obtained by the interaction of one of the several forms of energy like ultrasound, x-rays and γ-rays with the object under investigation. The specific physical phenomenon chosen depends on the character of the materials in the specimen being evaluated. Ultrasound tomography (UT) [11, 12] has been the choice for flaw detection in engineering materials since a long period. However, other NDE methods have become popular due to the characteristic property of bending of the ultrasound wave in heterogeneous media. Even then, UT has been shown to be a suitable, simple and economical procedure for prediction of various flaw characteristics, provided the properties of specimen material and defects are known to be approximately uniform (impedance mismatch is below ten percent) [3]. Acoustic wave attenuation and time-of-flight are the commonly acquired projection data used for reconstruction. With acoustic wave attenuation as the projection data, the reconstructed cross section is a visualization of the attenuation map. When the projection data is ultrasound time-of-flight, the reconstructed cross section is the image of slowness distribution. Slowness is the reciprocal of phase velocity of the acoustic wave through the object being scanned. In this work, reconstructions are based on time-of-flight data.

After the projection data is acquired through scanning the object, its radiating cross-section is treated as a function f(x, y) analogous to some characteristic material property of the object and is to be estimated using suitable procedures. The process is referred to as ’reconstruction‘ and the reconstructed cross-section is represented as an image. Mathematically computed tomography reconstruction can be expressed as: P=AF+E, in

which P is the acquired projection data vector that serves as input, A is the projection matrix, F is the unknown data vector to be reconstructed or found, and E is the reconstruction error vector. The objective of reconstruction is thus a problem of minimization of E [13] and several reconstruction procedures are in use with each of the methods having their pros and cons. Most tomographic reconstruction techniques in use can be categorized into one of the two major classes of reconstruction algorithms, the first being analytic or transform methods and the second class being iterative or expansion methods.

The basis for analytic methods, also called direct or transform methods, is the projection slice theorem or the central slice theorem (CST). The CST establishes the relationship between the 2D Fourier transform of the cross-section of an object and the scanned projection data. The theorem states that the one-dimensional Fourier transform of a projection obtained at an angle is the same as the radial or central slice taken through the two-dimensional Fourier domain of the object at the same angle. Filtered back projection (FBP) and convolution back projection (CBP) algorithms are the most extensively used analytic reconstruction procedures. Widely used iterative methods include algebraic reconstruction technique (ART) and its variants, simultaneous iterative reconstruction technique (SIRT), simultaneous algebraic reconstruction technique (SART), multiplicative algebraic reconstruction technique (MART), and simultaneous multiplicative algebraic reconstruction technique (SMART). The principal steps that are common to all iterative techniques are: (i) starting with an initial image guess that will be improved in an iterative manner, (ii) calculation of corrections aimed at improving the current image, (iii) application of the calculated corrections to the current image, and (iv) checking for convergence to terminate the iterative process. Different algorithms stated above differ in the way corrections are calculated and applied [3, 13-16].

Analytic procedures are very fast but are applicable only when complete projection data can be acquired along sets of straight ray paths. The disadvantage of iterative techniques being much slower is outshined by their ability to handle irregular sampling geometries, accommodate for refraction effects on scanning rays, reconstruct even when complete projection data is not available, and make use of any available apriori information in the reconstruction process. With iterative methods the reconstruction problem is no more than an analytic one but is converted to a combinatorial format which makes it appropriate to use GAs for solving the problem. Iterative methods also suffer from ill-conditionality and multi-modality due to discretization and here lays another motivation for using genetic algorithms. GAs are appropriate in solving continuous as well as discrete problems and ensure global convergence as the search is population based. On the other hand, reconstruction techniques based on classical optimization procedures might get stuck in a local optimum as they work on the basis of iteratively improving a single initial solution guess. GAs are search and optimization procedures modeled on the basis of natural selection principles of biological evolution. Introduced by John Holland and later extended by Goldberg, GAs have been applied to solve a wide range of optimization problems with objective functions that are continuous, discontinuous, stochastic, etc. In recent times, GAs are increasingly finding applications in the field of computed tomography as well [17-23]. The principal steps in the implementation of GAs which are evolutionary algorithms are illustrated in Fig. 1.

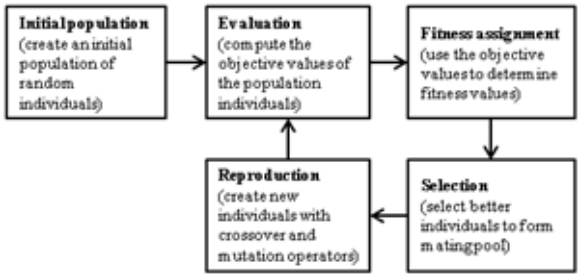

Fig. 1. Principal iterative steps in a genetic algorithm cycle.

Ultrasonic tomography that implements genetic algorithms for reconstruction of an object cross-section with an inclusion of known physical properties is discussed in [2]. A detailed description of various tomographic techniques including the mathematical basis and the applications of tomography is covered in [3]. A state-of-the-art one on various X-ray CT

technologies deployed in the manufacturing, food, electrical and electronic industry is provided in [5]. Also, it includes a brief overview of the technological advances as well as challenges to be addressed in industrial CT systems. Transmission tomography of isotropic materials (rubber, aluminium) using ultrasound TOF as the scanned data and the FBP algorithm for reconstruction is discussed in [6]. The application of X-ray CT for the assessment of the flexural behavior of the reinforced concrete is presented in [8]. The application of tomographic reconstruction for the inspection of nuclear fuel assemblies is discussed in [9]. The mathematics of ultrasound CT imaging using straight line reconstruction equations is presented in [10]. The basic principles of ultrasound tomography along with its applications, sensors technology and related software, that are key to its success are described in [12]. The mathematical concepts of popular reconstruction methods, the principal differences among each of them and their applications to different problems are detailed in [13-16]. The concepts and application of GAs for tomographic reconstructions are discussed in [17, 19-22].

Implementation of the proposed two stage ultrasound tomography process is detailed in the following sections. The first stage is concerned with the acquisition of the projection data (that in the present case is the simulated TOF data). The second stage is elucidated with the reconstruction of the object cross-section with GAs. The second stage of UT deals with a binary coded genetic algorithm reconstruction (BCGAR) procedure. The reconstruction results are obtained and conclusions are drawn for different test cases.

2. Stage-1 of UT - acquisition of projection data

Data acquisition is concerned with the collection of experimental or simulated projection data that serves as input to one of the reconstruction procedures employed for obtaining the cross-sectional image of the test specimen. In ultrasound tomography, the projection data is the attenuation of the wave energy and/or time-of-flight of ultrasound interacting with the material. This study uses the time-of-flight data and is based on the fact that the time-of-flight through a specimen without any defect will be different from the one when the specimen has a defect. In Fig. 2 two representative signals detected by ultrasound receivers after transmitting through two test specimens, one without defect and the other having an inclusion of a different material, are shown. With reference to an ultrasound signal collected by a receiver transducer, the arrival time corresponding to the first peak of the signal is taken as the TOF between the transmitter and the receiver as shown in Fig. 2.

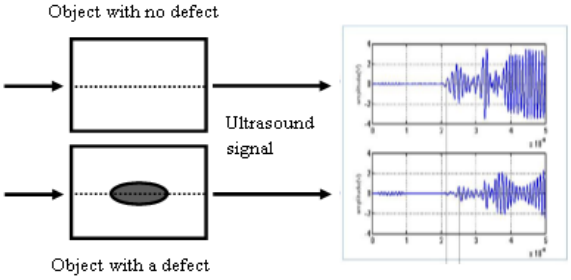

Fig. 2. Ultrasound signal from an object with no defect versus an object with a defect.

In this study, the TOF data is simulated following the procedure described in this section. In view of the availability of only finite amount of projection data that equals total number of ultrasound transmitter-receiver pairs, the tomographic reconstruction problem is solved by discretizing the specimen in the form of a grid of square cells with each cell assumed to represent the slowness value corresponding to specific materials. With a discretized model, the property being reconstructed can no longer be represented in a functional form and hence there is a need for representing the cross-section as an image.

In this application of Gas, referred to as binary coded genetic algorithm reconstruction (BCGAR) methodology, the specimen is assumed to have a maximum of three homogeneous materials known priori with one of the materials forming the objects mass and the other two distributed as inclusions. The TOF of ultrasound rays is simulated by representing the cross-section of specimen under consideration as a grid of integer values corresponding to different slowness values that characterize different materials. In this study, the base or parent material is represented by 0 (zero) while two different inclusion materials are represented as 1 (one) and 2 (two). Thus, programmatically any cross-section of the specimen is simply a square matrix of integers 0s (zeroes), 1s (ones), and 2s (twos). The size of this matrix is the

resolution of the image with each of the different materials distinguished by different colors.

Fig. 3(a and c) show how the cross-section of a representative specimen is stored as grids of integers while the corresponding display of the cross sections as images are illustrated in Fig. 3(b and d). It should be noted that this type of coding is slightly different from the conventional binary coding followed in a GA. While in the conventional binary GA all variables are coded as a string of binary digits, in the present problem, since priori information on the number of different types of materials that can be present is assumed to be known, each material type is distinguished from the other by assigning a different integer value. The integer value itself doe not change during the GA process as it represents the known slowness value of the corresponding material. Despite the differences the approach presented, it can be categorized as a binary GA based methodology in view of the functions of the GA operator's viz. the selection, crossover and mutation operators.

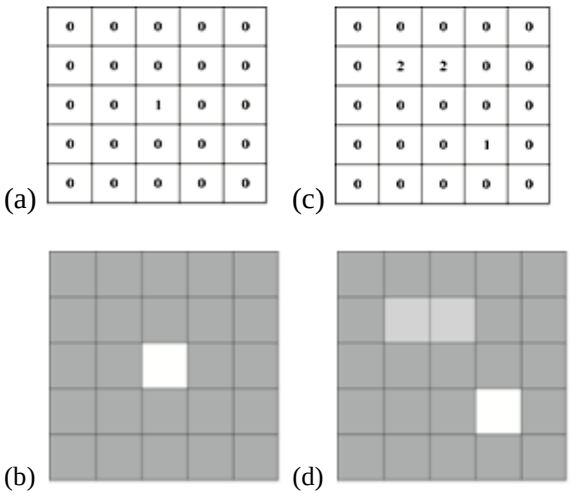

Fig. 3. Representations of specimens in the proposed algorithm; (a) & (c) representation in the program, and (b) & (d) visual display of the corresponding specimens.

Next, the TOF data is acquired by positioning a number of ultrasound transmitters and receivers (labeled as A, B, C, D) around the specimen in different configurations such that the maximum area could be covered by the rays and also sufficient and reliable data could be obtained. In this study, the transmitters and receivers are positioned following the modified cross-hole geometry having the advantage of acquiring more number of projections from the same number of transducers in addition to having symmetry in data acquisition and better angular coverage. Fig. 4 illustrates this feature.

Thus the ultrasound transducers (transmitters and receivers) can be arranged in six different ways referred to as config1, config2, config3, config4, config5 and config6 following the modified cross-hole geometry for collection of TOF data as illustrated in Fig. 5. Observe that in config1 arrangement the transmitters are on the left edge whereas the receivers are on the top edge of the specimen cross-section and the number of rays is equal to the number of transmitters (T) multiplied by the number of receivers (R). With the transducers arranged in different configurations (C) the total number of rays is equal to the number of rays in each configuration multiplied by the number of configurations in which the transducers are arranged. Thus, the input to the algorithm is the TOF values of all the rays from all the configurations put together. For example, considering $T=3$ transmitters, $R=3$ receivers and $C=6$ configurations, we get $T\times R\times C=54$ TOF readings, which are the input to the reconstruction algorithm. This is six times more than when the transducers are arranged following the simple cross-hole geometry shown in Fig. 4(a). It is evident that the ray density (number of rays in a grid cell) and resulting area of specimen covered increases immensely with an increase in the number of transducers per configuration. Though an increased coverage results in reconstructed images of better accuracy and higher resolution, with the resulting increase in volume of projection data acquired the reconstruction time of chosen algorithm also increases. This implies that one should carefully choose the number of transducers such that a balance is struck between the cost of transducers and the accuracy of reconstructions.

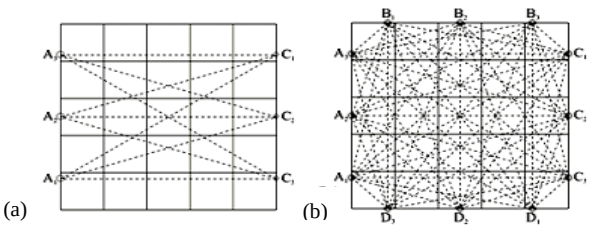

Fig. 4. Comparison of ray coverage; (a) cross-hole geometry and (b) modified cross-hole geometry.

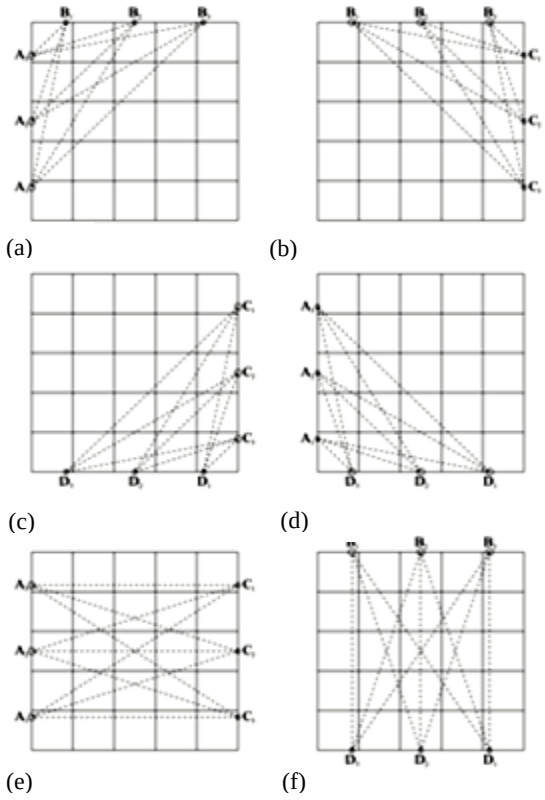

Fig. 5. Six different arrangements of ultrasound transmitters and ultrasound receivers, each one is referred to as a configuration; (a) config1, (b) config2, (c) config3, (d) config4, (e) config5 and (f) config6.

The effect of increasing the number of transducers on the ray density is shown in Fig. 6 for the case of a 5x5 grid with one, two, and three transducers per edge arranged according to the modified cross-hole geometry. Observe that for a specific grid size the number of rays through the cross-section is higher with higher number of transducers; and also note that for each grid size, there are minimum transducers to ensure passing of at least one ray through every grid cell. Thus, to ensure that the full cross-section is scanned during the data acquisition a study on the required number of transducers must be performed.

In the present study the TOF of ultrasound wave is simulated assuming that the ultrasound ray from a transmitter to a receiver follows straight paths without undergoing any bending. It is important to keep in mind that the assumption of straight rays is reasonably acceptable only when the variation in impedance within the specimen is small (less than 10%). In each configuration the transmitters are actuated in sequence one by one and the path taken by ultrasound rays from each of the transmitters to each of the receivers is traced.

For any given ray shown in Fig. 7 the simulated TOF is estimated using Eq. (1):

$$TOF_i = \sum_{j=1}^{N} D_{ij} S_j \tag{1}$$

Here, TOF_i is the time-of-flight of the i^{th} ray; D_{ij} is the distance travelled by the i^{th} ray in the j^{th} pixel; S_j is the slowness value of the wave in the j^{th} pixel in the direction of the ray path and N is the total number of pixels through which the i^{th} ray passes.

3. Stage-2 of UT - binary coded genetic algorithm reconstruction (BCGAR) procedure

A good number of reconstruction algorithms are available which differ primarily in the way the problem is formulated, and the solution is obtained. In the binary GA algorithm, the variables are coded as a string of binary digits and selection, crossover; and mutation operators are applied repeatedly until convergence on the population of binary strings takes place. In the present algorithm the cross-section is an array of integer values corresponding to slowness values (variable) represented as an image as illustrated in Fig. 3. The various GA operators are repeatedly applied on a population of such randomly generated arrays of integers till the cross-section of the object closely matches with the input projection data.

The salient features of the present reconstruction algorithm are given in the flowchart as shown in Fig. 8. Starting with a population of randomly generated solutions (cross-section of object), each member of the population is assigned a fitness value given by Eq. (2).

$$\phi(i) = \sum_{l=1}^{C}\sum_{j=1}^{T}\sum_{k=1}^{R}(TOF\_Pop^{(i)}(l,j,k) - TOF\_Specimen(l,j,k))^2 \tag{2}$$

Here, $\phi(i)$ represents the fitness of the i^{th} member of GA population, T is the number of ultrasound sources or transmitters, R is the number of ultrasound receivers or detectors and C corresponds to the number of configurations or arrangements of transmitters and receivers.

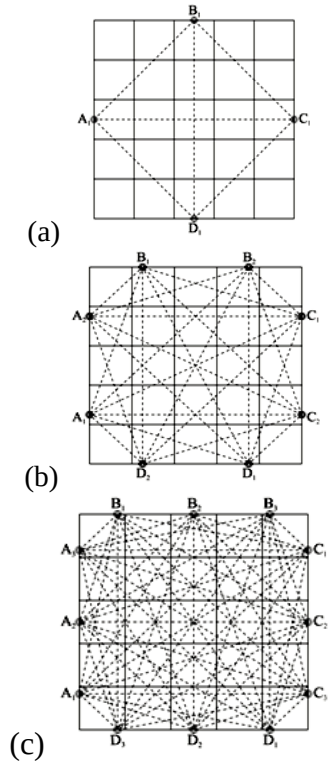

Fig. 6. Increase in ray density with an increase in the number of transducers per edge; (a) one transducer per edge (b) two transducers per edge, and (c) three transducers per edge.

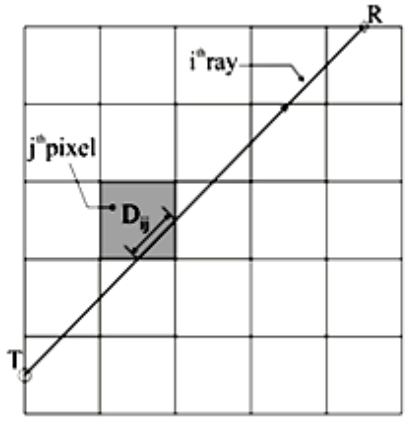

Fig. 7. Estimation of time-of-flight of a ray.

The fitness is taken as the sum of the squares of the deviation between the projected data (TOF) recorded from the specimen and the projected data of the population member being evaluated for the corresponding transmitter-receiver pair.
Observe that the initial population of solutions is randomly generated with a coarser starting grid size (SGS) and the grids are made finer and finer in steps during the reconstruction process of achieving the final solution. The best possible solution in the current step with a relatively coarser grid size is used as a reference or seed solution to randomly generate the population of solutions with a finer grid that is two times the previous grid size.

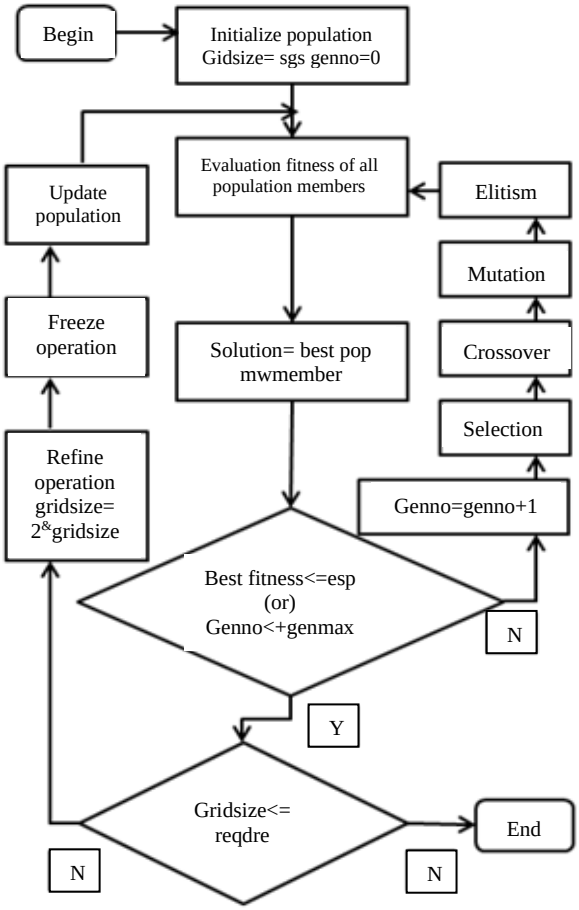

Fig. 8. The binary coded genetic algorithm reconstruction procedure (sgs: starting grid size).

The grid refinement process is repeated until the best possible solution with the final grid size is obtained. Thus, the possible location of the inclusions is identified quickly during the initial steps using coarser grids and later on the focus is shifted to the identification of the shape and the boundaries of those inclusions. The following sections give a detailed description of each of these steps.
The next step is the GA selection operation which ensures that better population members in the current population of solutions go into the mating pool using which child population is created by applying crossover and mutation operations. It is observed that the performance of

tournament selection is better when compared with the roulette wheel selection.

Following the selection operation, the population members in the mating pool are subjected to crossover operations resulting in the creation of new solutions. Three different crossover procedures viz., row crossover, column crossover, and block crossover operators are defined and applied on selected population members of mating pool. In the block crossover operation new solutions (children) are created by interchanging respective portions of the grids of the two identified mating pool members (parents). In the row crossover operation, corresponding rows of parents are interchanged to create child solutions. In the case of column crossover operation, respective columns of the chosen parents are interchanged to create child solutions. The parents from mating pool, the location and the size of corresponding portions to be interchanged in the chosen parents are all picked randomly. The row crossover, column crossover, and block crossover operations are illustrated in Fig. 9. It is observed that the performance of block crossover operator is better than the other two crossover strategies. In view of this, all results reported in this paper are those obtained by applying the block crossover operation.

Next, mutation operations are performed on a few randomly chosen individual child population members formed after crossover. Two different procedures of mutation operation viz., bitwise-mutation and block-mutation are defined and applied. In the bitwise-mutation operation chosen cells of the selected population member are randomly assigned a value that is different from the current value. In the block-mutation operation block of nine cells around the randomly chosen cell is updated with the cell value appearing most number of times in the block. The bitwise-mutation operation and block-mutation operation are illustrated in Fig.10 (a and b) respectively.

It is important at this stage that the good solutions resulting from crossover and mutation operations are carried forward through the following generations. Towards ensuring this, the concept of elite preservation is introduced into the algorithm.

For this the child population after mutation is merged with the initial (parent) population and few best population members amongst the merged population are picked which are referred to as elites. The elites thus picked are ensured to propagate through subsequent generations until a member superior to the elite in terms of fitness is generated. The best elite amongst the set of elites having the least fitness is saved as the solution with the current grid-size. In case the current grid-size equals the final grid-size, the solution obtained is reported as the final solution of the reconstruction process and the process terminated else current solution is refined as described in the following sections; and all previous steps applied repeatedly till the solution with required final grid-size is achieved.

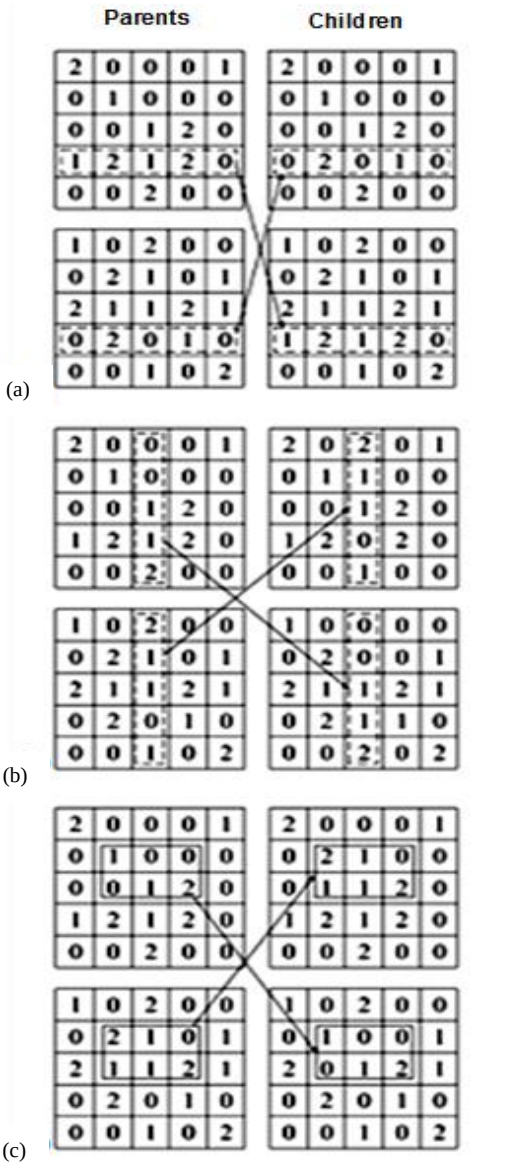

Fig. 9. Different crossover strategies; (a) row crossover (b) column crossover and (c) block crossover.

The resulting solution having a relatively coarser grid-size that is less than the final grid-size is now refined to a finer grid (larger grid-size), say double the current grid-size. This refinement is achieved by splitting each cell in the current solution into four cells and assigning each of these cells with the same value as in the parent cell being refined. Subsequent to the refining step certain cells are identified which need not be considered as variables in the next steps and all these are frozen applying a freeze operator. To accomplish this, the value of each cell in the refined solution is compared with the values in its surrounding eight cells. When there is a perfect match the value in the cell under consideration is frozen. The refining and freezing operations are as illustrated in Figs. 11 and 12 respectively.

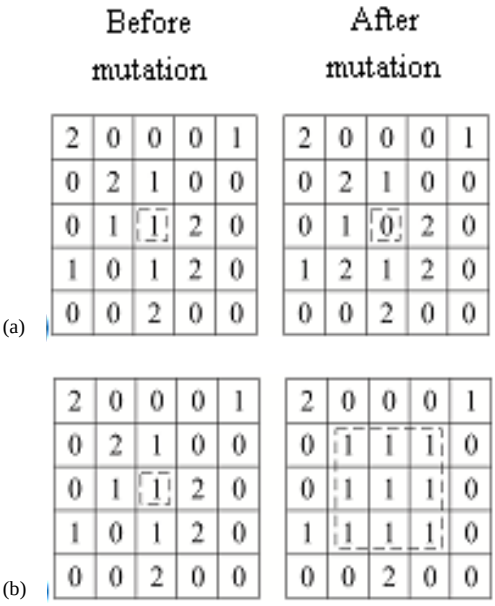

Fig. 10. Illustration of mutation operations; (a) bit mutation and (b) block mutation.

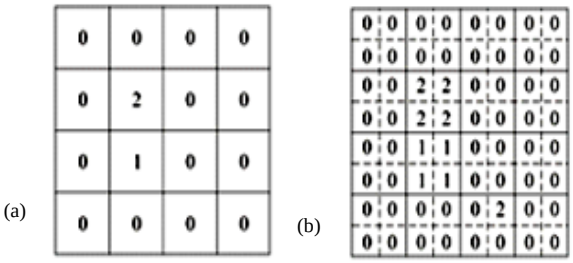

Fig. 11. Solutions; (a) before refine (b) after refine.

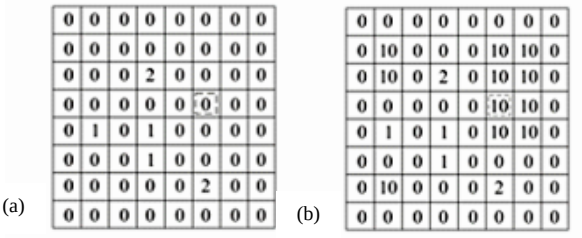

Fig. 12. Solutions; (a) before freeze and (b) after freeze.

The new finer grid solution obtained after refinement and freezing, is used as a reference or seed to create new initial population of solutions having the finer grid (grid-size of the seed solution). The initial population is updated with each member solution created by assigning random values to the unfrozen cells corresponding to the seed solution while leaving the values in the corresponding frozen cells unaltered. The various steps in GA procedure described are repeatedly applied until the final solution of required resolution (grid-size) is obtained. The maximum number of generations per step and the best misfit in a population being less than a certain specified value are used as the termination criterion for the reconstruction algorithm. For larger resolutions estimated time for reconstruction could also be used as the termination criteria.

4. Results and Discussion

4.1. Simulation of TOF data

Before proceeding to apply the present algorithm for the reconstruction of different cross-sections, it is necessary to estimate the minimum number of transducers required for simulating the projection data. All ray traces are performed neglecting the bending effects; and to justify this maximum contrast between the slowness of the three materials assumed is taken to be less than 10%. The slowness is nothing, but the inverse of wave propagation velocity which can be determined using the relation is given by Eq. (3).

$$c_l = \sqrt{\frac{E}{\rho}} \tag{3}$$

Here, c_l = wave propagation velocity in m/s, E = Young's modulus in GPa and ρ = density in kg/m^3.

Table 1 lists the properties of the materials used for simulating the projection data in the present study. Keeping in view of the assumption of straight rays, the three materials assumed to be present are either from one of the two groups: the first group consists of brass, copper and zinc and the second group consists of aluminum, iron, nickel and steel ensuring that the contrast in the slowness values is not more than 10 %.

Fig. 13 illustrates the ray coverage for two grid resolutions 5x5 and 10x10 for different number of transducers locations. The basis for deciding on the minimum number of transducers required is that at least one ray passes through each cell in the discretized model. This is because of the fact that each cell has one variable to be determined and every ray passing through the cell contributes to the calculation of that misfit function during the reconstruction process.

Observe that the ray coverage of the grid increases with the increase in the number of transducers locations. A careful scrutiny of the ray tracings reveals that for a 5x5 grid with only one transducer per side no ray passes through the grid cells in the corner. With an additional transducer, i.e. two transducers on each side, all grid cells are covered. For the case of 10x10 grid configuration, in addition to the corner grid cells there exist eighty grid cells through which no ray is traced.

Table 1. Properties of materials (viz., Young's modulus, E (GPa); density, ρ (kg/m^3); Poisson's ratio, μ; and wave propagation velocity, c_l (m/s)).

Mate-rial	E	ρ	μ	c_l
Brass	100	8400	0.36	3400
Copper	125	8900	0.35	3750
Zinc	100	7140	0.25	3700
Aluminium	72	2700	0.34	5160
Iron	210	7800	0.31	5180
Nickel	200	8860	0.31	4800
Steel	200	7800	0.30	5060

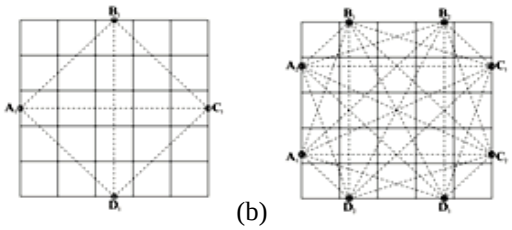

(a) (b)

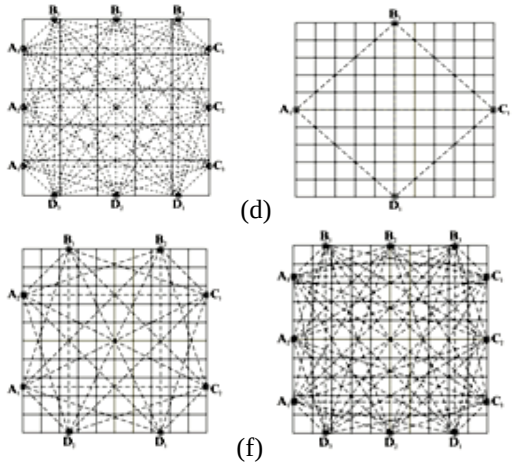

(c) (d) (e) (f)

Fig. 13. Ray coverage as a function of number of transducers per side; (a), (b), (c) one, two, and three transducers for a 5x5 grid and (d), (e), (f) one, two, and three transducers for a 10x10 grid.

A similar observation for the case of a 10x10 grid reveals that three transducers on each side ensure that all the grid cells are intercepted by at least one ray. A careful observation of the ray coverage illustrations in Fig.13(f) reveals that the rays from each of the transmitters in the mid side to the receivers in the middle of corresponding sides are coincident with the central grid lines. The TOF of such rays cannot be evaluated using the procedure outlined in section 2 as the rays do not pass through the inside of the grid cell but travel along the boundaries of the inclusion materials in the specimen. As a result, a conflict arises in choosing which slowness value is to be used. Thus, the minimum number of transducers required per side must be chosen not only based on the ray coverage but also only after ensuring that no ray coincides with the grid lines.

When one or more rays are found to coincide with the grid lines, the problem can be addressed in two ways; the first being relocating the transducers by a small offset on either side of the grid line and the second being to find the next minimum number of transducers that satisfy both the conditions of ray coverage through all grid cells and no ray coincides with the grid lines.

Thus, the minimum number of transducers required for simulating is two per side for a 5x5 grid and it is either three per side with the central transducer offset by a small value or four per side

for 10x10 grids. Thus, a detailed ray trace study must be performed before deciding on the minimum number of transducers for simulating the TOF data. Following the procedure, Table 2 gives the minimum number of transducers required such that every grid cell is intercepted by at least one ray for of 5x5, 8x8, 10x10, 16x16, 20x20, and 32x32 grids.

Table 3 presents a sample of complete simulated projection data for the case of a central offset square defect illustrated in Fig. 14(a). The slowness of the parent material and the inclusion is corresponding to that of nickel and steel respectively. With three transmitters and receivers located on each side following the modified cross-hole geometry, there is a total of fifty-four (54) rays each giving us one time of flight projection data. Table 3 shows the simulated TOF of first nine rays traced with transducers located as shown in Fig. 5(a).

4.2. Reconstructions of cross-sections

To demonstrate the efficacy of the present methodology, it is applied to reconstruct cross-sections of a number of specimens. The specimens have been chosen so as to demonstrate the capability of the algorithm in handling different grid resolutions, shapes of inclusions, and locations of inclusions, different inclusion materials, and contrast in the property being reconstructed. Results showcasing the variations are illustrated in Fig. 14. As outlined in Section 2, the specimens considered in the study are assumed to have at most three different materials whose slowness is known priori. In the representation of cross-sectional images, the three materials are shown in different colors/grey shades. The images in Fig. 14(a, b, c, e, f, g) correspond to specimens with only two different materials whereas the images in Fig. 14(d, h, i) correspond to specimens with three materials. While the images in Fig. 14(e), Fig. 10(f), and Fig. 10(j) correspond to configurations with a single inclusion located centrally, the images in Figs. 14(a) and Fig. 10(b) correspond to configurations with the inclusion located at some offset. The images in Fig. 14(c, d, h, i) represent the case of multiply located inclusions.

Table 2. Minimum number of transducers required per side for each of the grid resolutions.

Grid reso-lution	Min. transducers reqd.	Remarks
5x5	2	Acceptable
8x8	3	Some rays coincident with grid lines, to avoid the condition offset the transducers or use four transducers per side.
10x10		
16x16	7	Some rays coincident with grid lines, to avoid the condition offset the transducers or use eight transducers per side.
20x20		
32x32	14	Acceptable

Table 3. Simulated time-of-flight for the specimen in Fig. 14(a) with three transducers on each side arranged as shown in Fig. 5(a).

Config.	Ray no.	Ray from transmitter	Ray to receiver	Simulated tof (ms)
1	1	T1	R1	1.6467
	2		R2	1.8834
	3		R3	2.2836
	4	T2	R1	1.0214
	5		R2	1.3704
	6		R3	1.8834
	7	T3	R1	0.4568
	8		R2	1.0214
	9		R3	1.6467

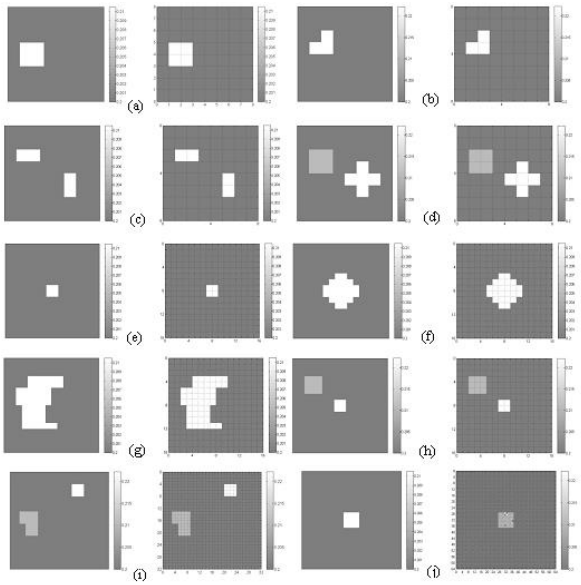

Fig. 14. Representative reconstructions; (a)-(d) 8x8 grid, (e)-(h) 16x16 grid, (i) 32x32 grid and (j) 64x64 grid.

Observe that the inclusions range from a simple square as in Fig. 14(a, d, e, h, i, j) to relatively complex shapes as in Fig. 14(b, d, f, g, i). In all the reconstruction studies the contrast in the specimen materials property, Young's modulus, has been taken to vary from 5% to 10% keeping in view of the fact that with larger contrast the bending of rays will be significant.

Each illustration comprises of two images: one on the left side is the actual specimen cross-section from which the input projection data is simulated; and one on the right shows the image of reconstructed cross-section. As outlined in section 2, the images are the distribution of slowness values across the cross-section. All results shown in Fig. 14 are obtained with the following common parameter settings: population randomly initialized with three different slowness values (corresponding to three different inclusion materials), size of the population is taken to be four times the final resolution (grid size), starting grid size of 8x8, and crossover probability of 0.8 and mutation probability of 0.01. The number of ultrasound transmitters and receivers for collecting the projection data is taken slightly on the higher side equal to half the desired resolution of specimen cross-section being reconstructed.

In Fig. 15, the improvement in fitness is shown for the case when the reconstruction algorithm starts with a randomly initialized population with grid resolution same as the final required resolution. This essentially means that throughout the reconstruction process the resolution of the population is the same as the one with which the initial population is generated. All the fitness history plots correspond to the reconstruction of the cross-section with materials distribution as illustrated in Fig. 15(a) at different resolutions. It can be seen that the cross-section considered has three different materials with two inclusions, the first being square located centrally and the second of a rectangular shape located at an offset. The plot in Fig. 15(b) is the fitness history plot for 8x8 grid resolution, while the plots shown in Fig. 15(c and d) are for 16x16 grid and 32x32 grid resolutions respectively. Observe that the fitness improvement follows a similar trend with higher generations required for finer grids. The reconstruction of 8x8 grid resolution required sixty generations and as mentioned earlier, the grid resolution of GA population all through the sixty generations remains the same which is equal to 8x8.

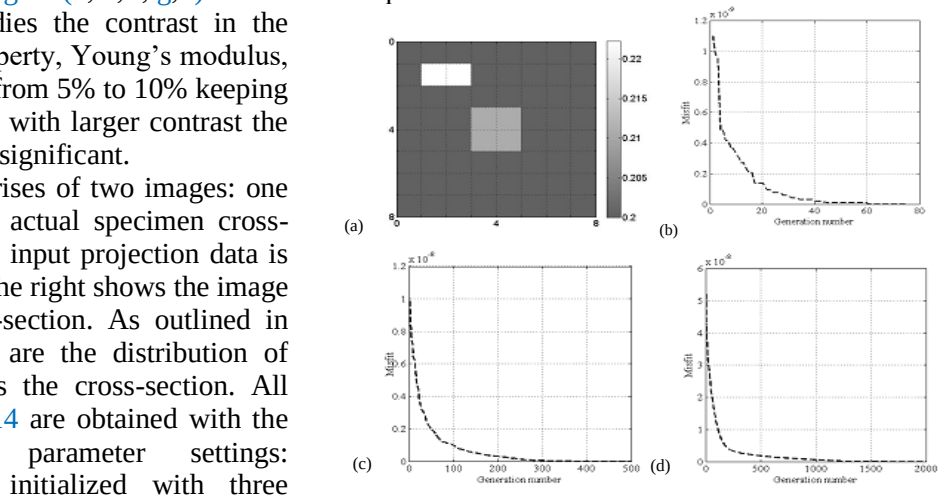

Fig. 15. Fitness history plots with a single step strategy; (a) reconstructed cross section (b) 8x8 grid (c) 16x16 grid, and (d) 32x32 grid.

Similarly, the grid resolution of the population is 16x16 in all the two hundred twenty generations it takes to converge for the case shown in Fig. 15(c) and it is equal to 32x32 all through the seven hundred generations it takes for reconstruction of a 32x32 grid resolution cross-section.

4.3. Multi-step strategy

Fig. 16 demonstrates the improvement of fitness with number of generations with a multi-step strategy. By multi step strategy we mean the grid resolution of the initial population is small which is increased in steps as the generations increase. Here we start with a coarse resolution (8x8) and proceed to finer resolutions (16x16, 32x32). At intermediate stages the grid is refined to finer grids moving towards the final resolution of the cross section being reconstructed. For example, observe from Fig. 16(c) that in reconstructing cross sections with 16x16 resolutions each grid cell of the best 8x8 solution obtained at the sixtieth generation is subdivided into finer grids of four cells each and all of them are deemed to have the same slowness value of that of the 8x8 mother grid cell.

The plots in Fig. 16(b, c, and e) are the fitness history plots when reconstructing cross-sections with 8x8, 16x16 and 32x32 grid resolutions

respectively. For the sake of clarity, Fig. 16(d and f) are the corresponding enlarged views of the portions of the plots enclosed in a rectangular frame as shown in Fig. 16(c and e).

Fig. 17 illustrates the reconstruction results when a multi-step strategy is applied for the reconstruction of a cross-section with 32x32 resolution. Fig. 17(a) shows the variation in misfit with each generation and the reconstruction results at intermediate stages are shown in Fig. 17(b, c and d). The image in Fig. 17(b) is the best solution with 8x8 grid resolution which serves as a seed to refine the population grid from 8x8 to 16x16. Fig. 17(c) shows the best solution obtained working with 16x16 grid which now serves as a seed for refining the population grid from 16x16 to 32x32 resolution. Fig. 17(d) shows the final reconstruction result.

4.4. Parametric studies

With a view to understand the sensitivity behavior of the present binary coded GA reconstruction algorithm to the parameters involved, parametric studies were performed for a range of values of the population size, probability of crossover, and the probability of mutation [18]. The results are shown in Fig. 18. Fig. 18(d and e) which is an enlarged view of the portion of Fig. 18(d) demonstrates the influence of population size on the nature of fitness with increasing number of generations. In addition, the influence of population size on the magnitude of the RMS error is also shown in Fig. 18(f).

While smaller values of both misfit and RMS indicate good reconstruction results, the value of misfit as defined by Eq. (2) does not give us any estimate of the deviation of the actual physical property distribution across the cross section. In order to correlate the misfit with the actual physical property RMS error is defined and calculated after the final reconstructed result is obtained. The RMS error is defined here, as the square root of the algebraic sum of the squares of deviation in physical property in each of the corresponding grid cells of the test specimen and the reconstructed cross sections.

It must be kept in mind that this value cannot be used as a fitness function while running a GA program since in a realistic situation one does not have any idea of the actual specimen cross section being reconstructed. It is observed that the performance of the present algorithm is poor with smaller population. One reason for this behavior possibly is that there is not enough diversity in the population with a small population size and the number of generations fixed is insufficient to converge within the specified acceptable deviation.

Fig. 18(g) demonstrates the increase in reconstruction time with an increase in population size. Thus, it should be kept in mind that though a higher population helps in converging to the desired solution it comes at the cost of a higher reconstruction time. Based on these observations, a population size equal to three to four times the required resolution is recommended and the same used in all the reconstructions illustrated in our study.

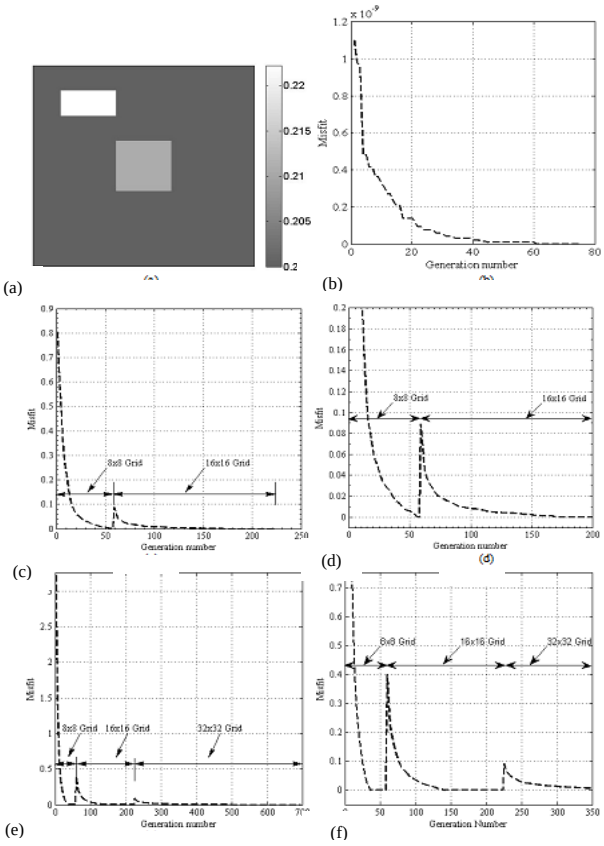

Fig. 16. Fitness history plots for different resolutions; (a) reconstructed cross section, (b) coarse resolution, 8×8grid, (c) finer resolution, 16×16grid with, (d) enlarged view, (e) finer resolution, 32×32grid with, and (f) enlarged view.

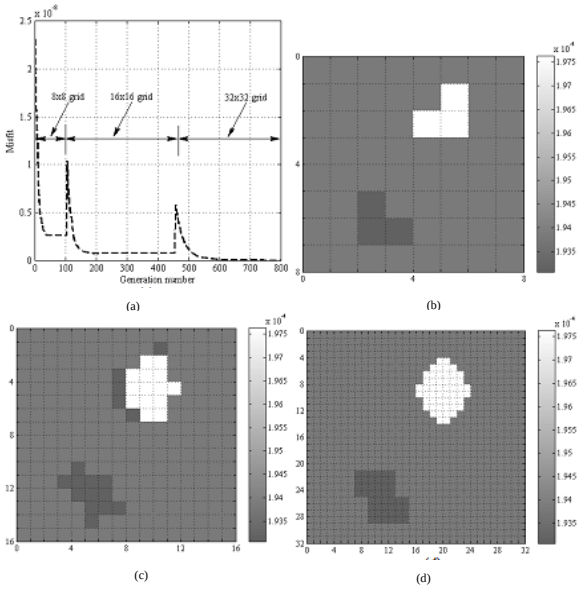

Fig. 17. Results of reconstructions with a multi-step strategy; (a) variation of misfit with each generation, (b) solution with 8×8grid, (c) solution with 16×16grid, and (d) final solution with 32×32grid.

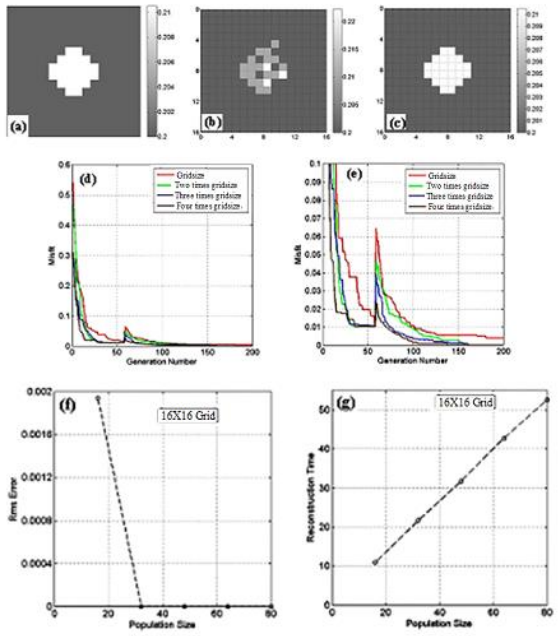

Fig. 18. Influence of population size on rms error and reconstruction time for a 16x16 cross section; (a) reconstructed cross section, (b) twice the grid size, (c) Thrice the grid size, (d) fitness versus number of generations with, (e) enlarged view, (f) RMS error with population size, and (g) reconstruction time with population size.

The reconstructed cross-section with the population size taken to be two times the grid size (2x16=32) and the one obtained with a population size more than three times the grid size (3x16=48 and above) are shown in Fig. 18(b and c) respectively. Fig. 18(a) illustrates the specimen cross section from which the projection data is collected.

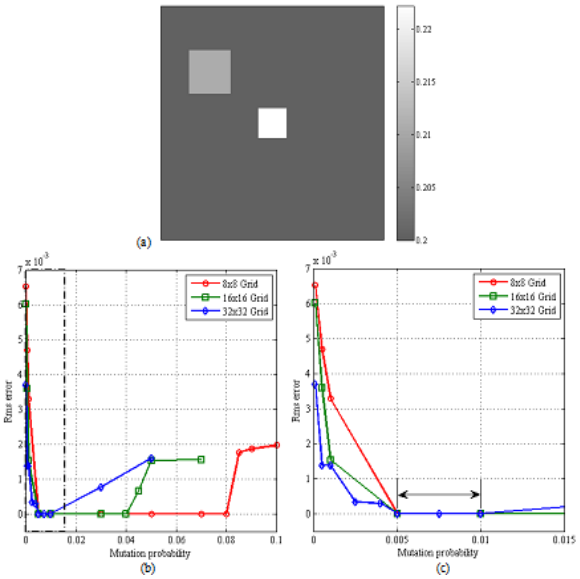

Fig. 19. Influence of probability of mutation for different grid sizes; (a) reconstructed cross section, (b) RMS error with mutation probability with, and (c) enlarged view.

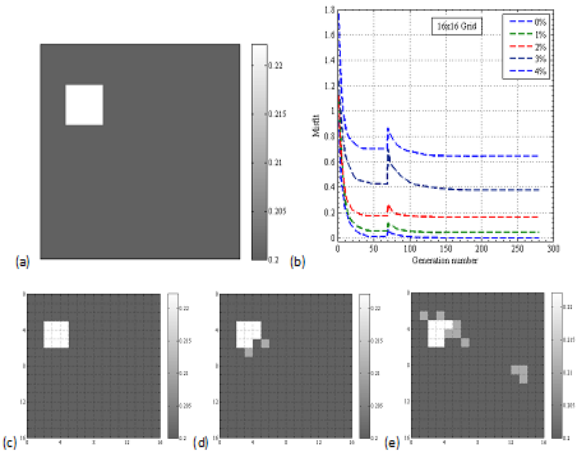

Fig. 20. Reconstruction results with noisy input data; (a) reconstructed cross section, (b) effect of noise in the projection data on the fitness history. Sample reconstructions for the case of, (c) 1% noise, (d) 2% noise, and (e) 3% noise.

4.5. Effect of noise in the projection data

Results obtained on the performance of present algorithm in handling the noise are illustrated in Fig. 20. The noise is introduced into the simulation data by increasing or decreasing at random each of the projection data by a certain percentage. This noisy projection data is given as input to the present algorithm and the reconstruction results analyzed. Fig. 20(b) demonstrates the effect of noise in the projection data on the fitness history when reconstructing the cross section shown in Fig. 20(a). It can be seen from Fig. 20(b) that with increasing percentage of noise, the reconstruction results deviate from the expected result and with a noise greater than or equal to 3% the reconstructions are unacceptable. Some sample reconstructions for the case of 1%, 2% and 3% noise are shown in Fig. 20(c, d and e) respectively.

5. Conclusions

A variation of binary coded genetic algorithm methodology for the tomographic reconstruction of material cross section is discussed and the results of numerical studies are presented. The reconstructions are performed with simulated time of flight data of ultrasound through the specimen under investigation. The method outlined assumes the specimen has at most three materials distributed across its cross section. The methodology is shown to be consistent in reconstructing specimens with different defects in terms of the material, shape, location and contrast in the reconstruction property. Parametric studies show that a population size of three to four times the grid size is appropriate. The mutation probability is observed to be inversely proportional to the grid resolution. The present method is shown to be capable of handling projection data contaminated with a maximum noise of 2%. The algorithm is limited in its application in that the ray tracing is performed by neglecting bending of rays and that the method assumes the availability of priori information of the materials in the specimen.

References

[1] K. R. Leonard, E. V. Malyarenko and M. K. Hinders, "Ultrasonic Lamb wave tomography", *Inverse Probl.*, Vol. 18, No. 6, No. 6, pp. 1795-1808, (2002).

[2] P. P. Delsanto, A. Romano, M. Scalerandi and F. Moldoveanu, "Application of genetic algorithms to ultrasonic tomography", *J. Acoust. Soc. Am.*, Vol. 104, No. 3, pp. 1374-1381, (1998).

[3] A. C. Kak and M. Slaney, *Principles of Computerized Tomographic Imaging*, Society of Industrial and Applied Mathematics, (2001).

[4] K. Bryant and R. Vaga, "Computer tomography from micro-electronics to assembled products", *Adv. Sci., Technol. Eng. Syst. J.*, Vol. 2, No. 3, pp. 932-936, (2017).

[5] L. De Chiffre, S. Carmignato, J. P. Kruth, R. Schmitt and A. Weckenmann, "Industrial applications of computed tomography", *CIRP Annals*, Vol. 63, No. 2, pp. 655-677, (2014).

[6] X. Teng and R. E. Green., "Ultrasonic tomographic imaging of defects in industrial materials", Review of Progress in Quantitative Nondestructive Evaluation, Eds. D. O. Thompson, D. E. Chimenti, Plenum Press, New York, pp. 889-896, (1993).

[7] P. Munshi, "A review of computerized tomography with application to two-phase flows", *Sadhana*, Vol. 15, No. 1, pp. 43-55, (1990).

[8] T. Ponikiewski and J. Katzer, "X-ray computed tomography of fibre reinforced self compacting concrete as a tool of assessing its flexural behavior", *Mater. Struct.*, Vol. 49, No. 6, pp. 2131–2140, (2016).

[9] S. J. Svärd, S. Holcombe and S. Grape, "Applicability of a set of tomographic reconstruction algorithms for quantitative SPECT on irradiated nuclear fuel assemblies", *Nucl. Instrum. Methods Phys. Res., Sect. A*, Vol. 783, pp. 128-141, (2015).

[10] J. F. Greenleaf, "Computerized tomography with ultrasound", *Proc.*

IEEE, Vol. 71, No. 3, pp. 330–337, (1983).
[11] B. Jiang, W. Zhao and W. Wang, "Improved ultrasonic computerized tomography method for STS (steel tube slab) structure based on compressive sampling algorithm", *Appl. Sci.* Vol. 7, No. 5, pp. 432, (2017).
[12] J. L. Rose, "A baseline and vision of ultrasonic guided wave inspection potential", *J. Press. Vessel Tech.*, Vol. 124, No. 3, pp. 273–282, (2002).
[13] C. Byrne, "Iterative algorithms in tomography", (2005).
[14] R. M. Lewitt, "Reconstruction algorithms: transform methods", *Proc. IEEE*, Vol. 71, No. 3, pp. 390–408, (1983).
[15] Y. Censor, "Finite series-expansion reconstruction methods", *Proc. IEEE*, Vol. 71, No. 3, pp. 409–419, (1983).
[16] E. F. Oliveira, S. B. Melo, C. C. Dantas, D. A. A. Vasconcelos and L. F. Cadiz, "Comparison among tomographic reconstruction algorithms with a limited data", *Proc. Int. Nucl. Atlantic Conf. - INAC 2011*, ISBN: 978-85-99141-04-5 (2011).
[17] N. N. Kishore, P. Munshi and M. A. Ranamale, V.V. Ramakrishna, W. Arnold, "Tomographic reconstruction of defects in composite plates using genetic algorithms with cluster analysis", *Res. Nondestr. Eval.*, Vol. 22, No. 1, pp. 31-60, (2011).
[18] K. Deb, *Optimization for Engineering Design: Algorithms and Examples*, Prentice Hall of India, New Delhi, (2004).
[19] R. S. Bichkar and A. K. Ray, "Tomographic reconstruction of circular and elliptical objects using genetic algorithm", *IEEE Signal Process. Let.*, Vol. 5, No. 10, pp. 248–251, (1998).
[20] K. J. Batenburg, "An evolutionary algorithm for discrete tomography", *Discrete Appl. Math.*, Vol. 151, No. 1-3, pp. 36 – 54, (2005).
[21] C. Valenti, "A genetic algorithm for discrete tomography reconstruction", *Genet. Program. Evolvable Mach.*, Vol. 9, No. 1, pp. 85–96, (2008).
[22] X. Yang, J. R. Ommen and R. F. Mudde, "Comparison of genetic algorithm and algebraic reconstruction for X-ray tomography in bubbling fluidized beds", *Powder Technol.*, Vol. 253, pp. 626-637, (2014).
[23] T. Weise, "*Global Optimization Algorithms-Theory and Application*", Version: 2009-06-26, (2009).

How to cite this paper:

Shyam Prasad Kodali and Boggarapu Nageswara Rao, "Tomographic reconstruction of isotropic materials using genetic algorithms with ultrasound time-of-flight projection data,", *J. Comput. Appl. Res. Mech. Eng.*, Vol. 11, No. 1, pp. 227-242, (2021).

DOI: 10.22061/JCARME.2020.4871.1596

URL: https://jcarme.sru.ac.ir/?_action=showPDF&article=1225